Variation in Upper Plate Crustal and Lithospheric Mantle Structure in the Greater and Lesser Antilles from Ambient Noise Tomography

David Schlaphorst[1], Nicholas Harmon[2], John-Michael Kendall[3], Catherine A. Rychert[2], Jenny S Collier[4], Andreas Rietbrock[5], Saskia Goes[4], Robert William Allen[6], Lidong Bie[7], Jon D Blundy[8], Ben Chichester[2], George Cooper[9], Richard Gareth Davy[4], Tim J Henstock[2], Stephen P. Hicks[4], Colin G. Macpherson[10], Ben Maunder[4], Julie Prytulak[10], Jeroen van Hunen[11], Jamie J Wilkinson[4], Marjorie Wilson[12], and Jon P Davidson[13]

[1]Instituto Dom Luiz (IDL), Faculdade de Ciências, Universidade de Lisboa
[2]University of Southampton
[3]University of Oxford
[4]Imperial College London
[5]University of Karlsruhe
[6]Imperial College, London
[7]Karlsruhe Insitute of Technology
[8]Oxford University
[9]Cardiff University
[10]University of Durham
[11]Durham University, UK
[12]University of Leeds
[13]Durham University

November 24, 2022

Abstract

The crust and upper mantle structure of the Greater and Lesser Antilles Arc provides insights into key subduction zone processes in a unique region of slow convergence of old slow-spreading oceanic lithosphere. We use ambient noise tomography gathered from island broadband seismic stations and the temporary ocean bottom seismometer network installed as part of the VoiLA experiment to map crustal and upper mantle shear-wave velocity of the eastern Greater Antilles and the Lesser Antilles Arc. We find sediment thickness, based on the depth to the 2.0 km/s contour in the Grenada and Tobago basins up to 15 km in the south, with thinner sediments near the arc and to the north. We observe thicker crust, based on the depth to the 4.0 km/s velocity contour, beneath the arc platforms with the greatest crustal thickness of around 30 km, likely related to crustal addition from arc volcanism through time. There are distinct low velocity zones (4.2-4.4 km/s) in the mantle wedge (30-50 km depth), beneath the Mona Passage, Guadeloupe-Martinique, and the Grenadines. The Mona passage mantle anomaly may be related to ongoing extension there, while the Guadeloupe-Martinique and Grenadine anomalies are likely related to fluid flux, upwelling, and/or partial melt related to nearby slab features. The location of the Guadeloupe-Martinique anomaly is slightly to the south of the obliquely subducted fracture zones. This feature could be explained by either three-dimensional mantle flow, a gap in the slab, variable slab hydration, and/or melt dynamics including ponding and interactions with the upper plate.

Hosted file

`agusupporting-information_word_template.docx` available at https://authorea.com/users/527361/

articles/604400-variation-in-upper-plate-crustal-and-lithospheric-mantle-structure-in-the-greater-and-lesser-antilles-from-ambient-noise-tomography

Variation in Upper Plate Crustal and Lithospheric Mantle Structure in the Greater and Lesser Antilles from Ambient Noise Tomography

D. Schlaphorst[1,2], N. Harmon[3], J.M. Kendall[4], C.A. Rychert[3], J. Collier[5], A. Rietbrock[6], S. Goes[5], and the VoiLA Team[†]

†The VoiLA Team:

R.W. Allen[5], L. Bie[6], J.D. Blundy[4], B. Chichester[3], G.F. Cooper[7], J.P. Davidson[8], R.G. Davy[5], T.J. Henstock[3], S.P. Hicks[5], C.G. Macpherson[8], B. Maunder[5], J. Prytulak[8], J. van Hunen[8], J.J. Wilkinson[5,9], M. Wilson[10]

[1]Instituto Dom Luiz (IDL), Universidade de Lisboa, Portugal.

[2]School of Earth Sciences, University of Bristol, UK.

[3]Ocean and Earth Science, University of Southampton, National Oceanography Centre, Southampton, UK.

[4]Department of Earth Sciences, University of Oxford, UK.

[5]Department of Earth Science and Engineering, Imperial College London, London, UK.

[6]Geophysical Institute (GPI), Karlsruhe Institute of Technology, Karlsruhe, Germany.

[7]School of Earth and Environment, Cardiff University, Cardiff, UK

[8]Department of Earth Sciences, Durham University, Durham, UK.

[9]Department of Earth Sciences, Natural History Museum, London, UK.

[10]School of Earth and Environment, University of Leeds, Leeds, UK.

Corresponding author: David Schlaphorst (dschlaphorst@fc.ul.pt)

Key Points:

- With land and ocean bottom seismometers, we map significant variations in sediment/crustal thickness in fore- and back-arc in new detail.
- Sediments thickens towards the southern arc, whereas crustal thickness increases towards the north.
- Volatile input and pathways depend on slab seafloor morphology, 3D flow and/or melt ponding beneath the upper plate redistributing melt.

Abstract

The crust and upper mantle structure of the Greater and Lesser Antilles Arc provides insights into key subduction zone processes in a unique region of slow convergence of old slow-spreading oceanic lithosphere. We use ambient noise tomography gathered from island broadband seismic stations and the temporary ocean bottom seismometer network installed as part of the VoiLA experiment to map crustal and upper mantle shear-wave velocity of the eastern Greater Antilles and the Lesser Antilles Arc. We find sediment thickness, based on the depth to the 2.0 km/s contour in the Grenada and Tobago basins up to 15 km in the south, with thinner sediments near the arc and to the north. We observe thicker crust, based on the depth to the 4.0 km/s velocity contour, beneath the arc platforms with the greatest crustal thickness of around 30 km, likely related to crustal addition from arc volcanism through time. There are distinct low velocity zones (4.2-4.4 km/s) in the mantle wedge (30-50 km depth), beneath the Mona Passage, Guadeloupe-Martinique, and the Grenadines. The Mona passage mantle anomaly may be related to ongoing extension there, while the Guadeloupe-Martinique and Grenadine anomalies are likely related to fluid flux, upwelling, and/or partial melt related to nearby slab features. The location of the Guadeloupe-Martinique anomaly is slightly to the south of the obliquely subducted fracture zones. This feature could be explained by either three-dimensional mantle flow, a gap in the slab, variable slab hydration, and/or melt dynamics including ponding and interactions with the upper plate.

1 Introduction

Subduction zones play a key role in driving plate tectonics, delivering slabs and their volatile elements to the mantle. Slab dehydration during the subduction process results in melt generation, which rises and eventually leads to the formation of volcanic island arcs. Hydration may vary along strike depending on slab crustal structure, fracture zones and sediment packages (Stern, 2003). However, the relative importance of these delivery mechanisms and the exact pathways of hydration and melt to surface volcanism are not well known. Imaging variations in the crust and lithospheric mantle in these regions offers insights into subduction processes and the formation of continental crust through arc volcanism. Seismic methods offer the best potential to image the arc lithosphere at the scale of tens of kilometres required. However, many studies of island arcs are limited by the restriction of land stations to mostly small arc islands (noisy) in a linear alignment or sparsity in linear offshore active-source seismic profiles. A further limitation on our understanding of subduction processes is that until recently, seismic studies have focussed mostly on Pacific subduction zones (see Melekhova et al. (2019) for lists of references). The Volatile Recycling in the Lesser Antilles (VoiLA) experiment is focussed on the Lesser Antilles Arc (LAA), where slow-spread lithosphere are subducted (Goes et al., 2019).

Many subduction zones show complex crust and mantle structure in the upper plate, with along-arc heterogeneities, such as mantle xenolith mineral composition and discontinuity depths (e.g., Boynton et al., 1979; Kodaira et al., 2007; Melekhova et al., 2019; Schlaphorst et al., 2018; Shillington et al., 2004). These are likely related to factors including variation in slab age, convergence rate and direction. In addition, it is likely that oceanic plates are more hydrated at slow spreading centres that at fast spreading centres (e.g., Davy et al., 2019) and the distribution of hydration can vary significantly along the arc (e.g., Schlaphorst et al., 2016). Erupted magmas from Guadeloupe and Dominica show a high δ^{11}B anomaly that is indicative of dewatering of serpentinized oceanic crust (Cooper et al., 2020). In recent years, differences in the nature and intensity of the aforementioned slab heterogeneities between regions of subduction of fast spreading plates (mostly located in the Pacific) and those of slow spreading plates (found in the Atlantic) have become increasingly clear (Bie et al., 2020; Cooper et al., 2020; Melekhova et al., 2019; Schlaphorst et al., 2018).

Here, we image the LAA and the eastern Greater Antilles (GA), a slow-subduction zone located at the eastern boundary of the Caribbean plate, using ambient noise tomography (ANT). ANT has been used in a recent study to map shear-wave velocities in the Caribbean (Arnaiz-Rodríguez et. al, 2020). In our study, data are recorded by a dense network of permanent land stations and additionally an array of oceanic bottom seismometers deployed during the VoiLA experiment (VoiLA; Goes et al., 2019), which increases resolution in the fore- and back-arc. Previous studies have investigated the crustal structure in this area via active source imaging and receiver functions (e.g., Allen et al., 2019; Arnaíz-Rodroguez et al., 2016; Boynton et al., 1979; Chichester et al. , 2020; Christeson et al., 2008; Dorel et al, 1974; Kopp et al., 2011; Melekhova et al., 2019; Pauldron et al., 2020; Schlaphorst et al., 2018; Sevilla et al., 2012) but the inter-island subsurface is poorly studied so far. Our aim is to image the shallow mantle and crust, investigating variations in sediment accumulation, crustal thickness and the velocity structure in the uppermost mantle across the arcs.

2 Tectonic Setting

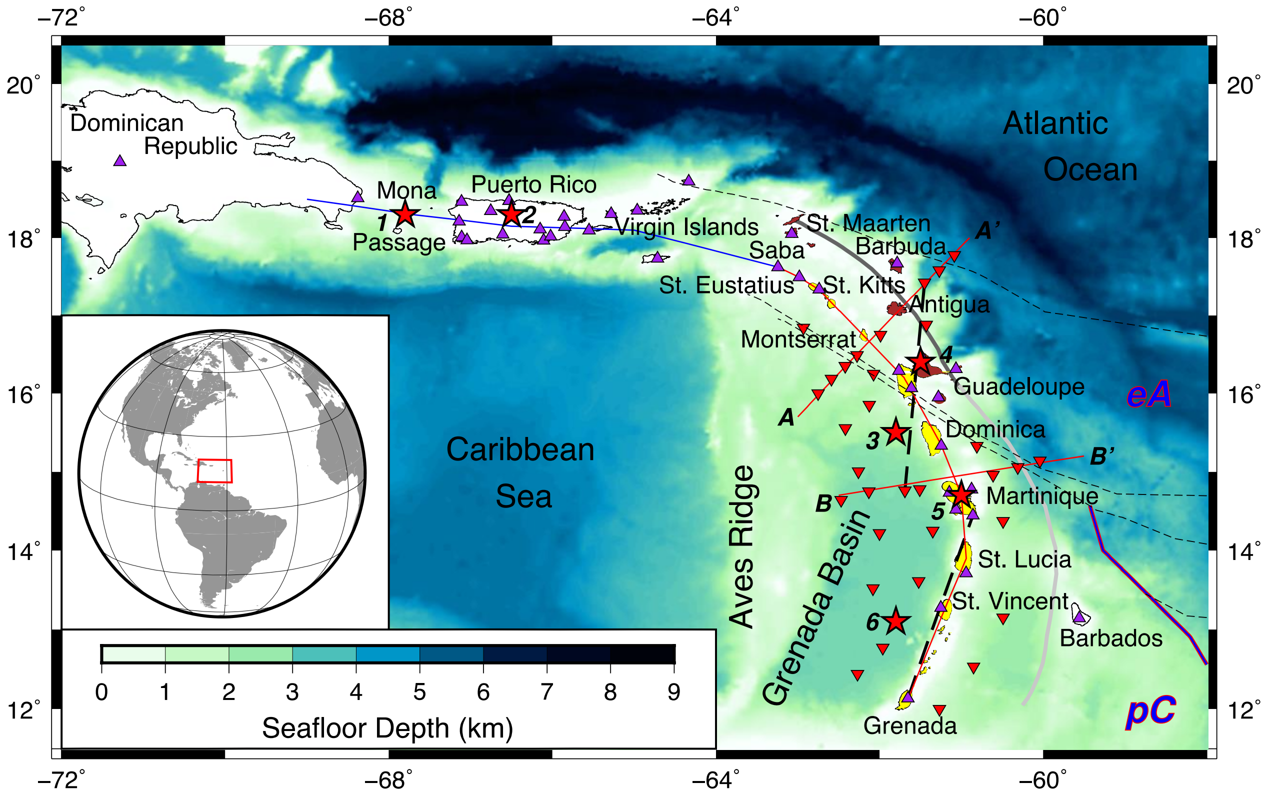

Figure 1: Map of the LAA and the GA, including bathymetry and the locations of seismic island stations (purple triangles) and OBS stations (red inverted triangles). Station details can be found in Supplementary Table S1. The global location of the area is shown in the inset. The islands of the LAA are coloured in yellow (Volcanic Caribbees) and brown (Limestone Carribees), and the islands of the GA are white. The location of the OA is shown as a thick grey line with the southern buried part depicted in a lighter grey (Allen et al., 2019). Thin black dashed lines indicate fracture zones and the blue line with red outline show the boundary between the proto-Caribbean (pC) and equatorial Atlantic (eA) seafloor (Cooper et al., 2020). Thick black hashed lines indicate the paths of the cross-correlated data from island–island and OBS–OBS station pairs for the examples shown in Fig. 3. Red stars show the locations of the individual results (Fig. 8). Thin solid lines indicate positions of the cross-sections (Fig. 10) for the GA (blue) and LAA (red).

The eastern GA and LAA (Fig. 1) are located on the northern and eastern margin of LIP-thickened (large igneous province) oceanic crust of the Caribbean plate (Mauffret & Leroy, 1997). The origin and evolution of the Caribbean plate since the Cretaceous can be inferred from its crustal structure. Over the past 100 My the Caribbean plate has been moving eastwards relative to both the North and South American plates. This motion has been accommodated by subduction, and strike-slip boundaries, resulting in large scale shear zones through continental/oceanic crust and arc volcanism at various times and places on the plate margin

(Boschman 2014). Subsequently, sedimentation and tectonism have obscured many of these features, therefore making it difficult to unravel a complex history.

The eastern GA area includes the islands of Hispaniola, Puerto Rico and the Virgin Islands, which together form the Northern Caribbean Plate Boundary Zone. The islands are located on microplates, which override the North American Plate and the thickened Caribbean Plate in two subduction zones to the north and to the south (Dolan et al., 1998). Dominated by a left-lateral east-west strike-slip motion, the complex tectonic setting of the area includes oblique convergence of the North American Plate, as well as a pull-apart basin in the Mona Passage between Hispaniola and Puerto Rico (Dolan et al., 1998; Masson & Scanlon, 1991; Ten Brink, 2005). Furthermore, a potential slab gap east of Puerto Rico has been suggested in several studies, based on bathymetry, seismic reflection profiles and gravity measurements (Ten Brink, 2005), as well as shear-wave splitting (Meighan et al., 2013; Schlaphorst et al., 2017).

The volcanic islands of the LAA have been formed by slow (18 to 20 mm/yr; DeMets et al., 2000), westward subduction of the North and South American plates beneath the Caribbean Plate (Wadge & Shepherd, 1984). The entire arc extends about 800km in a mostly north-south orientation. To the north and south it is bound by the GA and the South American continent, respectively. To the west it neighbours the Grenada Basin and the Aves Ridge (Boynton et al., 1979; Christeson et al., 2008), an abandoned, Mesozoic volcanic arc. The basin forms a depression characterised by a flat bottom in the south with depths down to 3km that spans a region of roughly 150 by 600km along the curved outline of the LAA and has formed due to north-south striking back-arc spreading while the so-called outer arc (OA; Fig. 1) was active (Allen et al., 2019; Bouysse, 1988; Padron et al., 2020).

The surface expression of the present-day arc comprises eleven major islands and the smaller Grenadine islands between St. Vincent and Grenada. Due to a spatial and temporal variations in magmatic output, the size and spacing of the volcanic islands varies. Around the island of Dominica, the LAA bifurcates to the north: the western active limb (the Volcanic Caribbees) includes the western part of Guadeloupe, as well as Montserrat, St. Kitts, St. Eustatius and Saba; the inactive eastern limb (the Limestone Caribbees) includes the eastern part of Guadeloupe, as well as Antigua, Barbuda and St. Martin (Bouysse et al., 1990). The Limestone Caribbees are part of the old OA that continues to the south buried under sediments from the Barbados accretionary prism (Allen et al., 2019). Due to the curvature of the present-day arc, a systematic change in subduction can be observed, with increased strike-slip movement especially towards the northern end (DeMets et al., 1994, 2000). A further variation along the arc can be observed includes the sedimentary load of the incoming plate. Sediment input from the South America continent is blocked by the presence of the east-west trending Tiburon Ridge and other submarine highs giving a much thicker sediment cover in the south. However, it is possible that a major part of these clastic sediments is accreted rather than subducted, forming the Barbados accretionary prism (e.g., Faugères et al., 1993). The orientation of the Wadati-Benioff zone along the arc also shows a significant change and thickens towards the south. The top of the subducting slab can be inferred from seismicity, lying at a depth of roughly 120km beneath the islands of the LAA (Bie et al., 2020). Finally, there is a change in the age and origin of the plate along strike, with the proto-Caribbean lithosphere subducting ahead of the South American oceanic lithosphere south of Dominica and lithosphere generated at the Mid-Atlantic Ridge (MAR) subducting to the North (Cooper et al., 2020).

3 Approach and Method

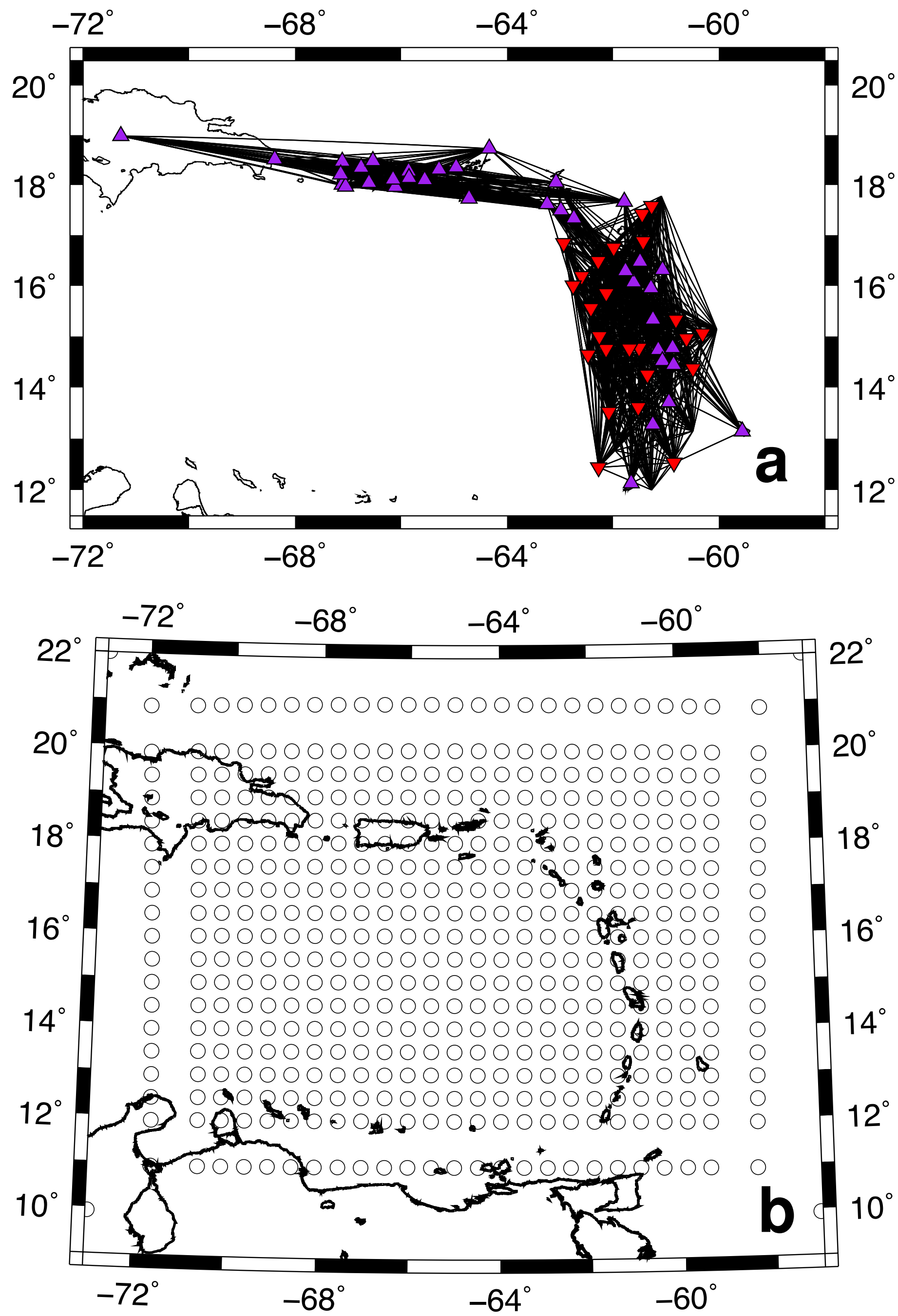

Figure 2: Station pairs and nodal parameterisation. a) Map showing the station pairs used, including locations of seismic island stations (purple triangles) and OBS stations (red inverted triangles). Note that due to the addition of OBS stations the tomography can be carried out on a broader range in the LAA. b) Nodal parameterisation used in this study with nodes being indicated by the white circles. The spacing is 0.5° by 0.5°. The outside nodes are placed at a 1° distance and are included to dampen any potential heterogeneity outside the region of interest.

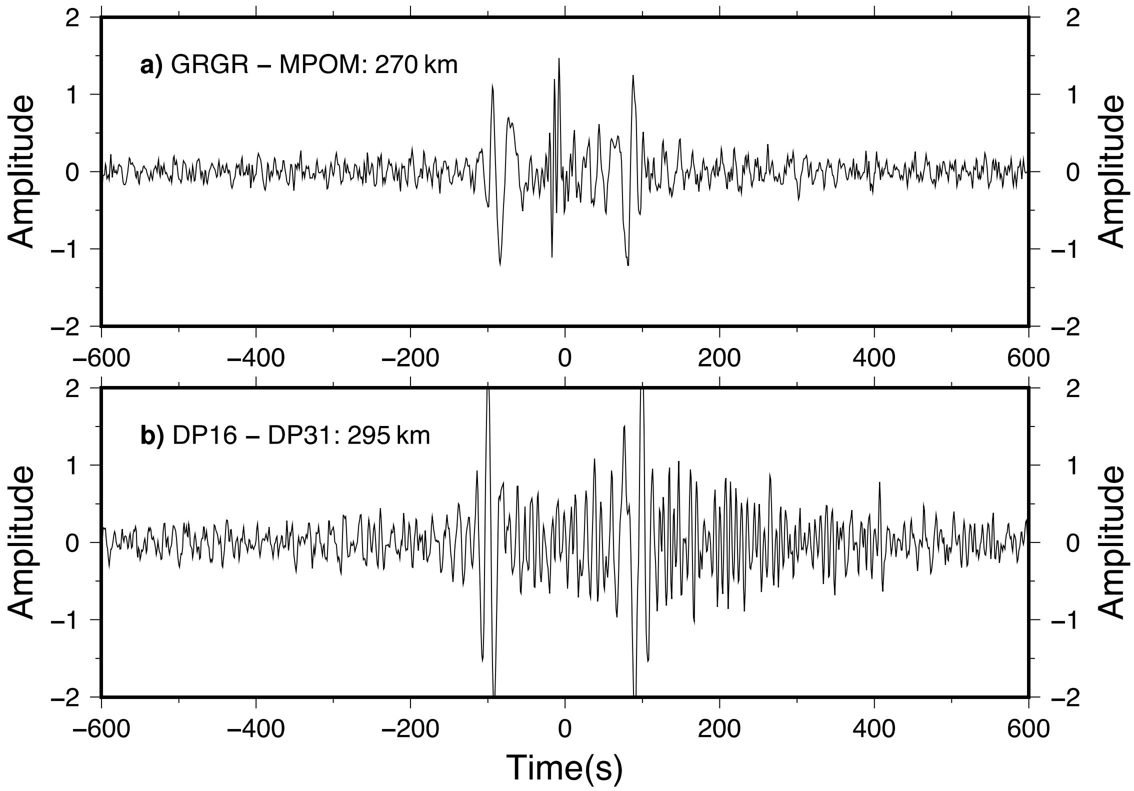

Figure 3: Examples of 1-year symmetric vertical-vertical component cross-correlations of island stations (a) and temporary VoiLA OBS (b). The additional peak in (a) around 0 s is a result of data gaps and does not affect the tomography results. For the corresponding station–station paths see Figure 1.

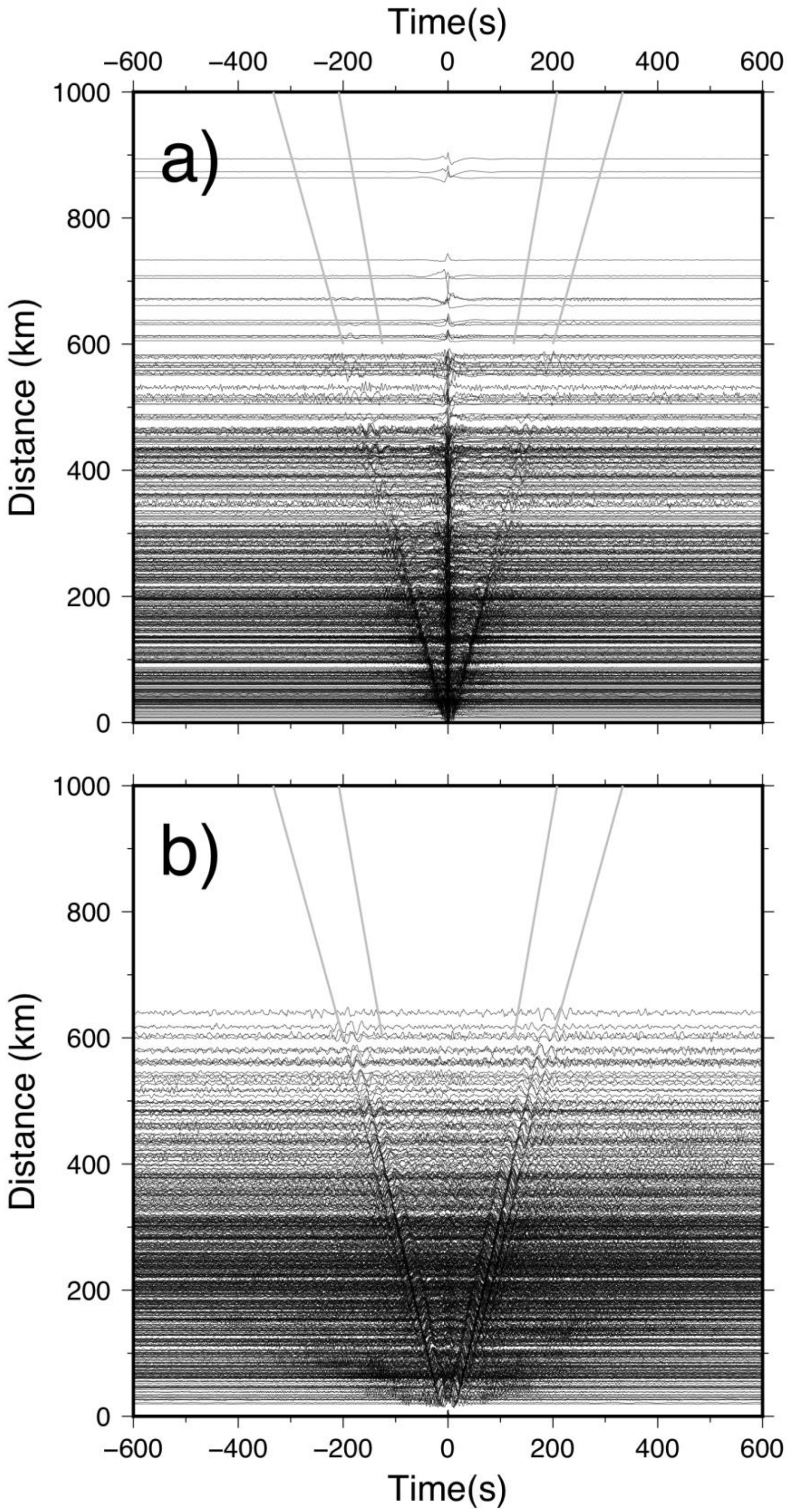

Figure 4: see following page for caption. (Please be aware that this is a version with compressed quality for the Word document.)

Figure 4: Symmetric cross-correlations of the vertical-vertical component of all station pairs ordered by station distance for the island stations (a) and the VoiLA OBS (b). The data are bandpass filtered using a 4th-order Butterworth bandpass filter between 1.5 s and 50 s. The Rayleigh waves can be seen with linear moveouts. The cross-correlation of the island stations introduces large peaks at around 0 s (a) due to data gaps. The cross-correlated data of the OBS shows a higher amount of noise in the codas (further away from 0 s than the Rayleigh wave onsets; b). However, these features do not affect the measurements, since we are focusing on onsets in a window around the Rayleigh wave arrivals using a search window from 3.0 km/s to 4.8 km/s. The search window is indicated by grey lines beyond a distance of 600 km.

We use ambient noise cross correlations to perform Rayleigh wave tomography across the region, following the technique laid out by Sabra et al. (2005) and Shapiro et al. (2005). We use continuous data recorded at 32 OBS stations from the VoiLA project and 39 permanent land stations (Fig. 2a; Suppl. Tab. S1). The OBS were deployed in 2016 and operational for a time span of approximately 14 months, although deployment times vary from station to station (Collier, 2017). We use data from land stations data covering the same time span as the OBS network. Additional land station data were used from an interval of equal length in the years 2012/2013 to test for temporal stability. The method follows the basic processing scheme of Bensen et al. (2007) and in particular the scheme presented by Harmon and Rychert (2016).

The data are processed in 1-day windows, which allows for faster computation. Here, we concentrate on the vertical components, which show Rayleigh waves most clearly and in general offer the highest signal-to-noise ratio (e.g., Tanimoto, 2006; Webb, 2007; Mordret et al., 2013a). Before the noise cross-correlation functions (NCF) are generated, the data are downsampled to 1 Hz. At this frequency, the noise field is predominantly generated by oceanic noise, which shows relatively random source distribution (e.g., Harmon et al., 2008; Mordret et al., 2013b; Yang & Ritzwoller, 2008). Any mean or trend is removed from the raw traces and amplitudes are normalised by a running average filter. Spectral whitening is applied in a frequency band from 0.01 to 0.33 Hz by using the magnitudes of the smoothed Fourier coefficients of the amplitude spectrum as inverse weights for the complex spectrum, acting as a spectral normalisation (Bensen et al., 2007; Harmon et al., 2008).

Station pairings for the NCFs are chosen so that their minimum distance is larger than three times the wavelength, which counteracts near-field effects, while simultaneously allowing for phases to become distinguishable (Bensen et al., 2007; Harmon et al., 2008). The interstation distance range is between 30 km and 1000 km (Figs. 3, 4). In this study we do not cross-correlate OBS data with permanent station data due to back scattering effects at the islands. However, both cross-correlation datasets are combined afterwards, resulting in a total number of 1906 pairs (496 OBS pairs and 1410 permanent station pairs; Fig. 2a). The 1-day NCFs for a particular station pairing are then stacked. Due to the linearity of cross-correlation the result is the equivalent of a longer timeseries (Bensen et al., 2007).

The waveforms in the positive (“causal”) and negative (“acausal”) parts of the resulting vertical-vertical (ZZ) component of the NCF are equivalent to waves travelling in both directions between the stations. Summing the positive and the time-reversed negative parts results in a causal, symmetric NCF that represents an average of both parts (Bensen et al., 2007; Harmon et al., 2010; see also Figs. 3, 4). The slight asymmetric behaviour of the traces can be explained by inhomogeneous distribution of noise sources (Bensen et al., 2007; Mordret et al., 2013b), though at low frequencies this is expected to be a minor problem. We window the symmetric NCF using a Tukey window with a 40s falloff before unwrapping the phase to determine individual cycle ambiguities (Harmon & Rychert, 2016).

To estimate the average phase velocity structure of the region we approximate the real component of the Fourier transformed NCF using Bessel functions of the first kind, representing 2-dimensional noise source distribution. Harmon et al. (2010) show that this approximation is valid at the longer periods used in this study (>7s). The minimum variance determines the best fit and thus the best amplitude/phase velocity pair. We search for phase velocities in an interval of expected values (3.0 km/s to 4.8 km/s) and select periods ranging from 6 s to 50 s. To investigate the lateral phase velocity structure at different depths we introduce nodal parametrisation (Fig. 2b) and use 2d sensitivity kernels in our tomography method (see Harmon & Rychert (2016) for more details).

Shear-wave velocity inversions are conducted at various locations throughout the region of interest. The starting model is built of 54 layers; the first represents a water layer with changing thickness (Becker et al., 2009); the second represents a sediment layer again with changing thickness based on a global sediment thickness compilation (Divins, 2003); the remaining layers have fixed thicknesses (two 1 km at the top and 5 km below). All layers have a v_P/v_S ratio of 1.8 as an average of the ratio that varies laterally and with depth (Schlaphorst et al., 2018). We also include a low velocity zone in the asthenospheric mantle wedge beneath 70 km (Chichester et al., 2019; Cooper et al., 2020). Densities are calculated using relationships for crustal (Christensen & Salisbury, 1975) and mantle layers (Birch, 1961). We replace the water layer with the sediment values for regions above sea-level. Due to the marine environment of the region we expect low shear-wave velocities in the upper layers, which are prone to be water saturated (Mordret et al., 2014). An upper limit for S-wave velocity of 4.5 km/s in the crust and 4.85 km/s in the mantle is fixed in the inversion.

We examine the resolution of the phase velocity map inversion using a checkerboard test (Fig. 5). As input we use 1˚x1˚ checkerboard anomalies for 14 and 20 s periods and a 1.5˚x1.5˚ anomalies for 30 and 45 s periods. These periods were chosen to cover the entire range used. The anomaly strength is set to ±1% around the average velocity for each period, which is a good proxy for the strength of anomalies that can be expected in this study. The synthetic phase is calculated using the finite frequency kernels from each period. We also include a small percentage of random noise to the synthetic data, which is equivalent to the amount of noise in the real data.

Checkerboard tests reveal a good recovery of features along the LAA for all periods especially inside the network, due to the dense station distribution. The resolution in the eastern GA is poorer due to the confined distribution of station locations along the islands (in the LAA this is greatly improved due to the inclusion of off-arc OBS data).

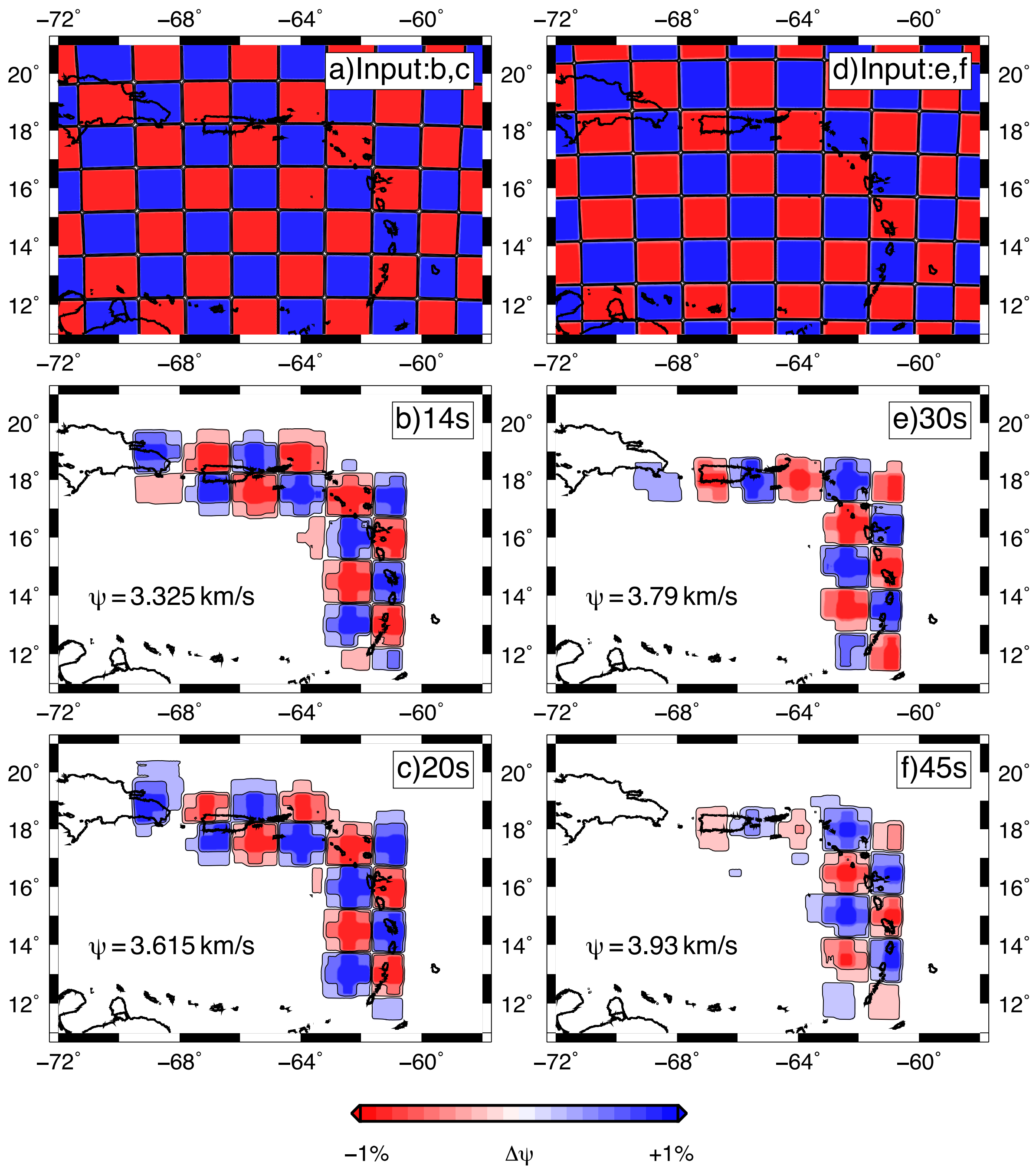

Figure 5: Checkerboard recovery tests for periods shown in Figure 7. Checkerboard length scales are 1˚x1˚ for the shorter periods and 1.5˚x1.5˚ for the longer periods. For every period, the average velocities (here called ψ) match the ones obtained as averages of the respective periods in the real data. Note that random noise is present in both input models (a, d) but visibility in this figure depends on the colour scale.

4 Results

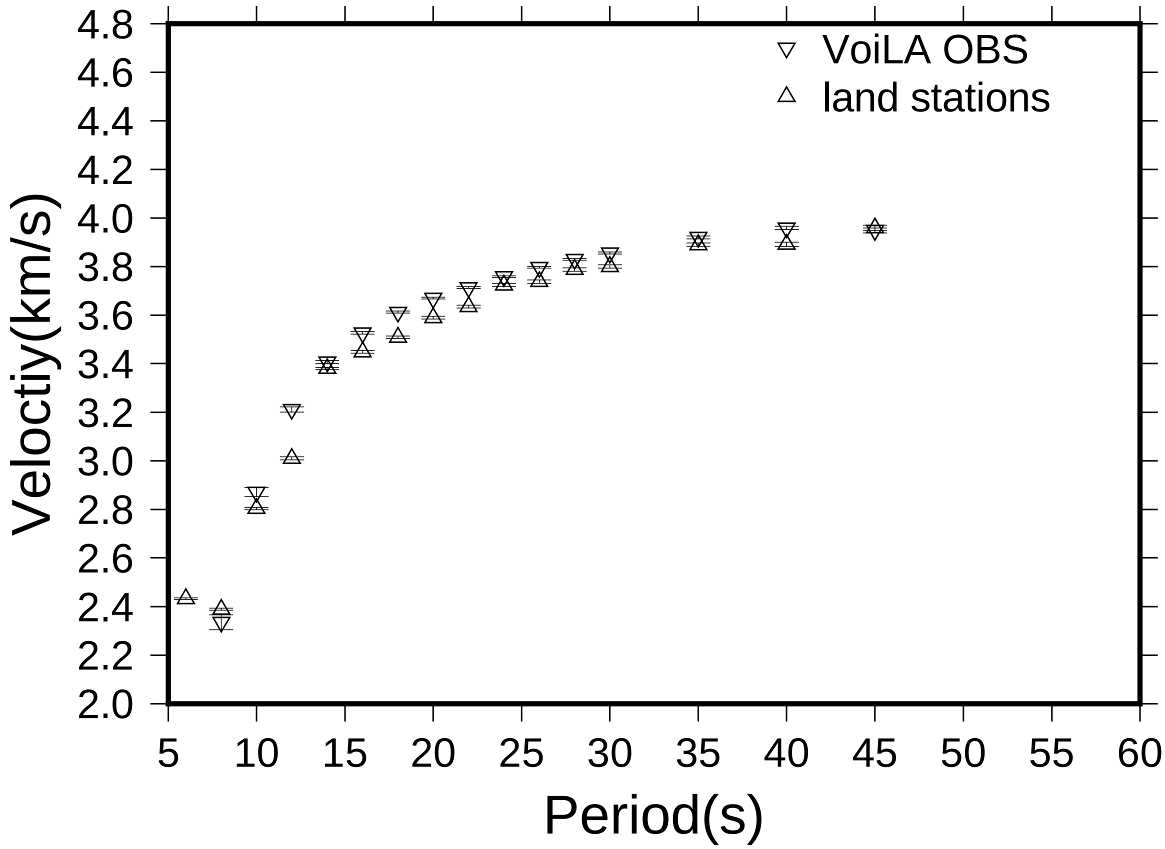

Figure 6: Measured average phase velocities and their uncertainties. Due to their lack of coherency periods shorter than 14 s were not used for further investigation.

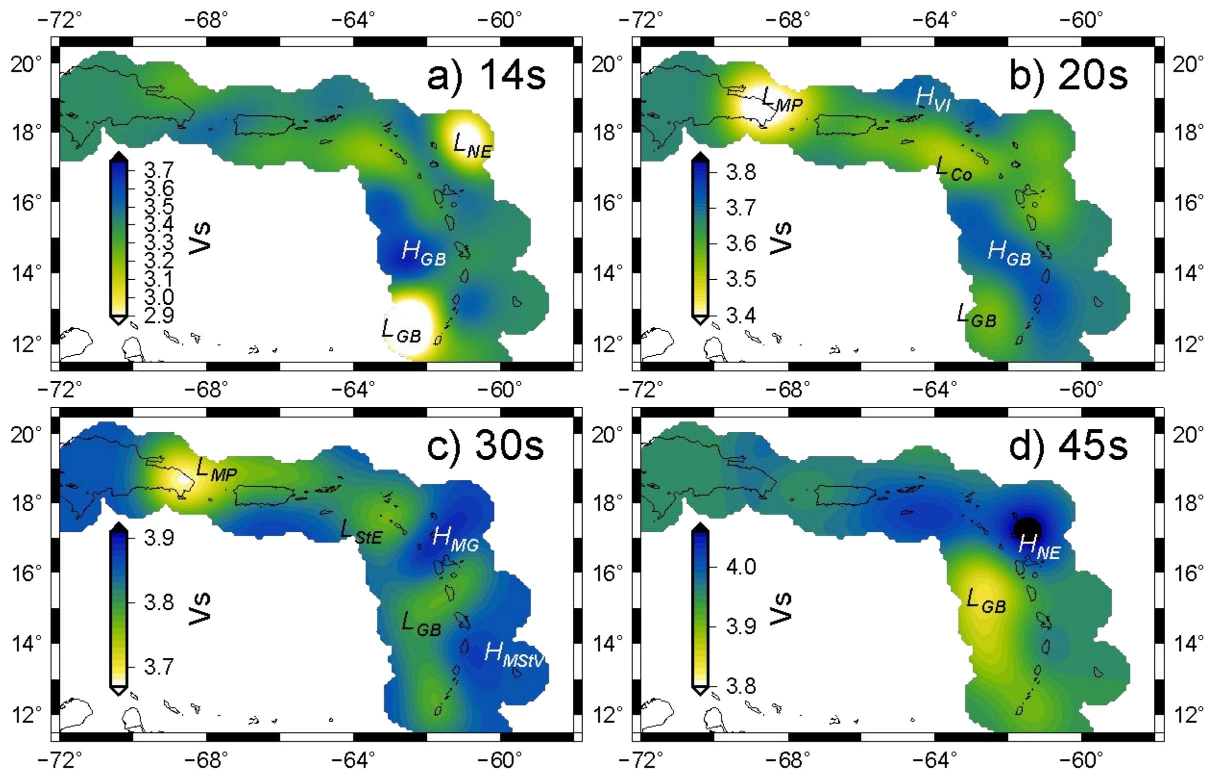

Figure 7: Surface wave tomography maps. Regions of strong low and high velocity anomalies are labelled and are discussed in the text. Note that the colour scale is changing for each individual panel to facilitate the visibility of variations.

The average phase velocities determined from the OBS and land stations (Fig. 6) show good agreement at most periods, with the dispersion recorded by the OBS being slightly faster (up to 0.05 km/s). Both dispersion curves show a faster velocity increase at shorter periods, reaching a plateau at longer periods that are sensitive to the upper mantle. At periods shorter than 14 s the agreement is worse. This is likely due to the OBS data sensing inherently different structure from both the fore- and back-arc and rapid variation in water depth. We therefore exclude these periods in the following analysis and concentrate on the longer periods from 14 s to 45 s.

Phase velocity maps for different periods generated from the combined dataset of permanent and OBS stations are shown in Figure 7. At 14 s the average Rayleigh wave phase velocity for the GA and the LAA is around 3.3km/s (Figs. 6, 7a). Two strong low-velocity anomalies can be observed in the southern Grenada Basin (L_{GB}; 2.56 ± 0.08 km/) and northeast of the northern end of the LAA (L_{NE}; 2.78 ± 0.09 km/s). Furthermore, a large region of high velocities of up to 3.71 ± 0.06 km/s show in the northern part of the Grenada Basin (H_{GB}).

At 20 s the average Rayleigh wave phase velocity for the GA and the LAA is around 3.6 km/s (Figs. 6, 7b). An elongate high-velocity anomaly can be identified, which spans the area north of the Grenada Basin, a continuation of the high-velocity anomalies observed at 14 s, and meets the LAA around St. Lucia and St. Vincent, where it reaches phase velocities of up to 3.75 ± 0.07 km/s (H_{GB}). This creates a tripartite pattern along the arc with higher velocities in the centre and significantly lower values to the north (Martinique to Saba) and to the south (the Grenadines and Grenada). A further smaller high-velocity anomaly is located north of the Virgin Islands, with phase velocities of up to 3.72 ± 0.10 km/s (H_{VI}). Three major low-velocity anomalies can be identified. One is located at the eastern end of Hispaniola at the beginning of the Mona Passage and shows phase velocities as low as 3.33 ± 0.08 km/s (L_{MP}). Two further minor low-velocity anomalies with phase velocity values of around 3.4 km/s are visible in the back-arc corner between the GA and the LAA (L_{Co}; 3.51 ± 0.08 km/s) and the southern LAA back-arc (L_{GB}; 3.56 ± 0.08 km/s).

At 30 s the average phase velocity value is 3.8 km/s (Figs. 6, 7c). The strong low-velocity anomaly beneath eastern Hispaniola also stands out at this period (L_{MP}; 3.68 ± 0.07 km/s). Along the LAA, a patchy pattern is observable with low-velocity anomalies in the north around St Eustatius (L_{StE}; 3.77 ± 0.07 km/s), as well as the centre around Dominica (3.78 ± 0.04 km/s) and in the south around Grenada (3.78 ± 0.08 km/s), the latter two being connected via the Grenada Basin (L_{GB}). These three lows are intercepted by areas of high-velocity anomalies around Montserrat to Guadeloupe (H_{MG}; 3.89 ± 0.05 km/s), as well as Martinique to St. Vincent (H_{MStV}; 3.87 ± 0.08 km/s).

At 45 s the average phase velocity value is 3.9 km/s around the LAA with slightly higher values of 4.0 km/s in the GA (Figs. 6, 7d). A round area of high velocity can be observed in the north-eastern part of the LAA (H_{NE}; 4.08 ± 0.05 km/s). In the west of the LAA a low-velocity anomaly is located in the southern two-thirds of the Grenada Basin (L_{GB}; 3.83 ± 0.06 km/s). The feature is in a similar location as the low velocity region at 30 s. The area north of Guadeloupe consistently shows higher average shear-wave velocities under the arc with the feature extending to western Puerto Rico.

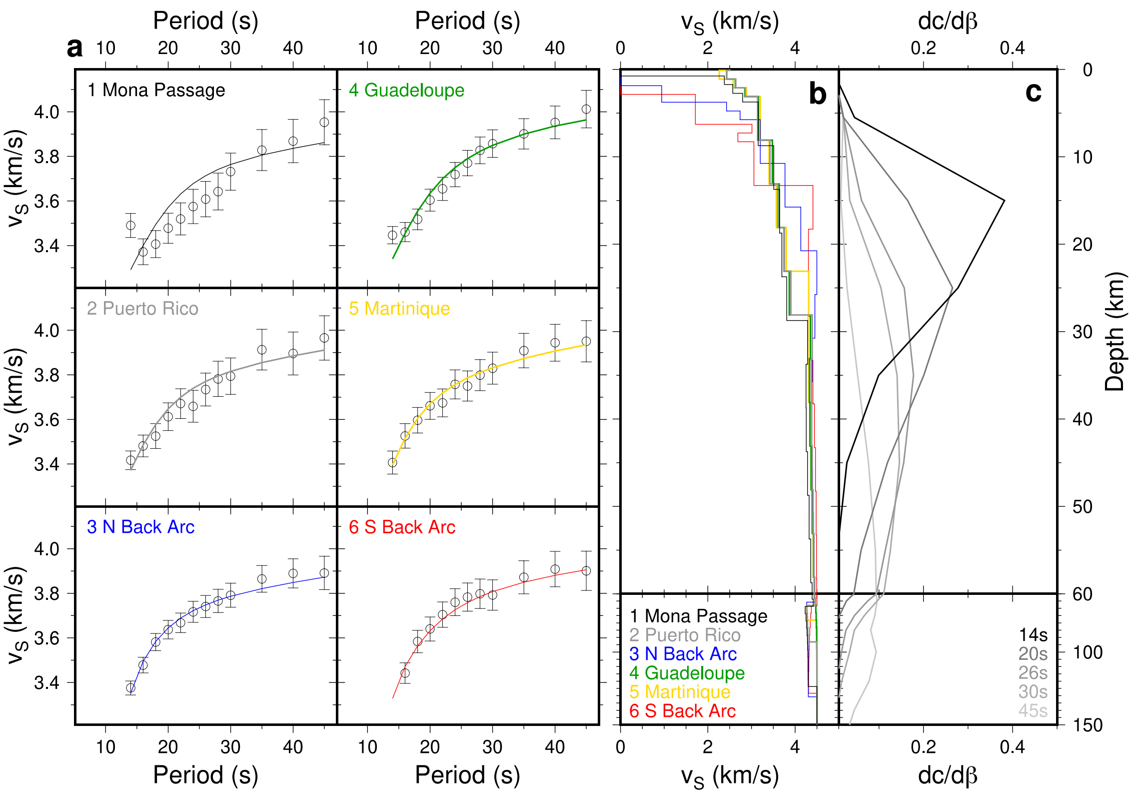

Figure 8: Dispersion results for 6 locations around the GA (Mona Passage, Puerto Rico) and LAA (Northern Back-arc, Guadeloupe, Martinique, Southern Back-arc). The locations are indicated in Figure 1. (a) Model of shear velocity dispersion curve (line) based on 1-D phase velocity estimates (black circles with error bars). (b) Resulting best fit shear velocity model. (c) Rayleigh wave sensitivity kernels with depth at different periods.

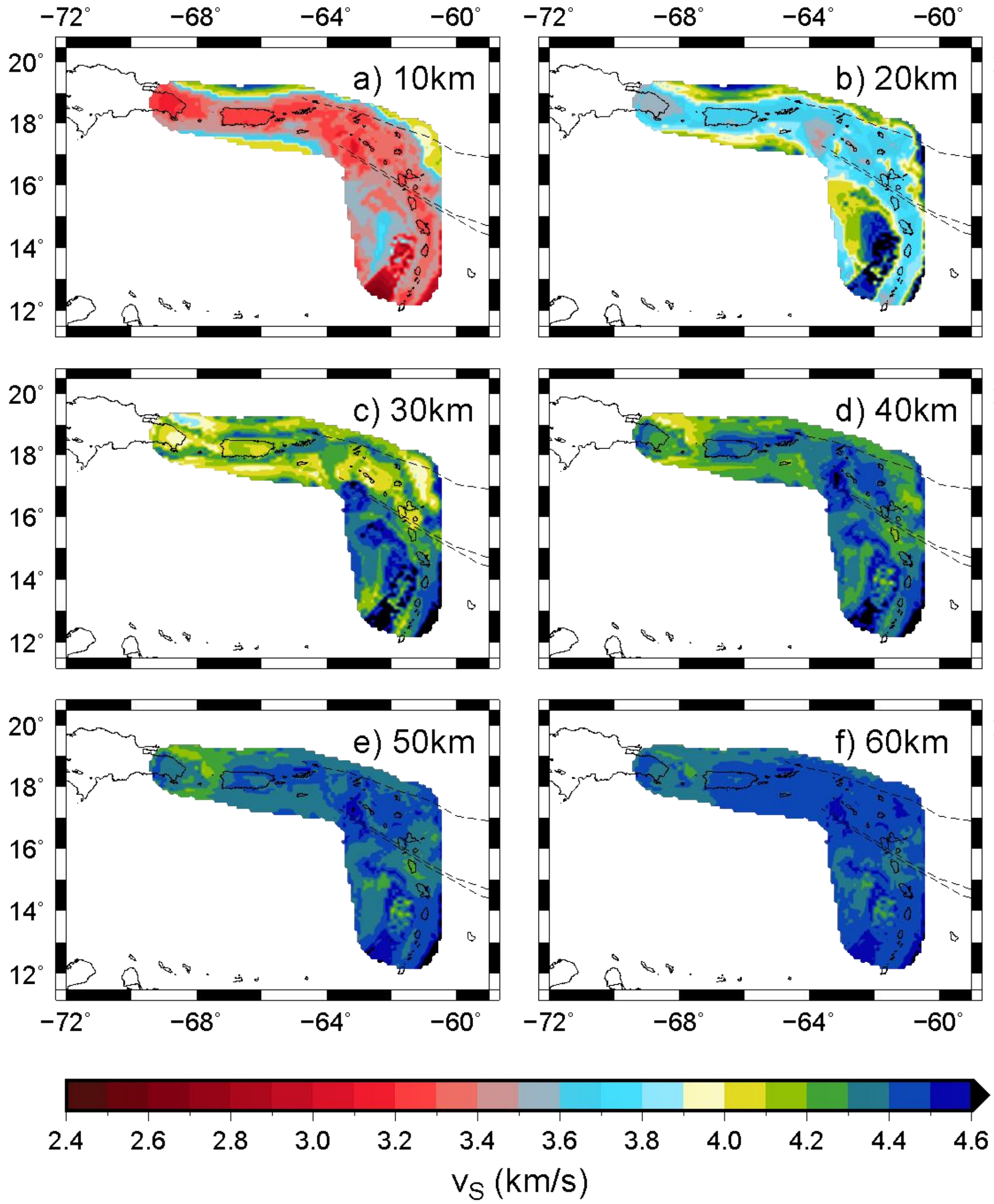

Figure 9: S-wave velocity depth slice maps in the GA and the LAA. The red-to-light blue scale indicates S-wave velocities commonly associated with crustal values, whereas the yellow-to-dark-blue scale indicates values associated with mantle values. White areas depict regions without results, due to either a high misfit in the inversion or location with great distance from the station pair paths (see Fig. 2a). Thin black hashed lines indicate fracture zones (Cooper et al., 2020).

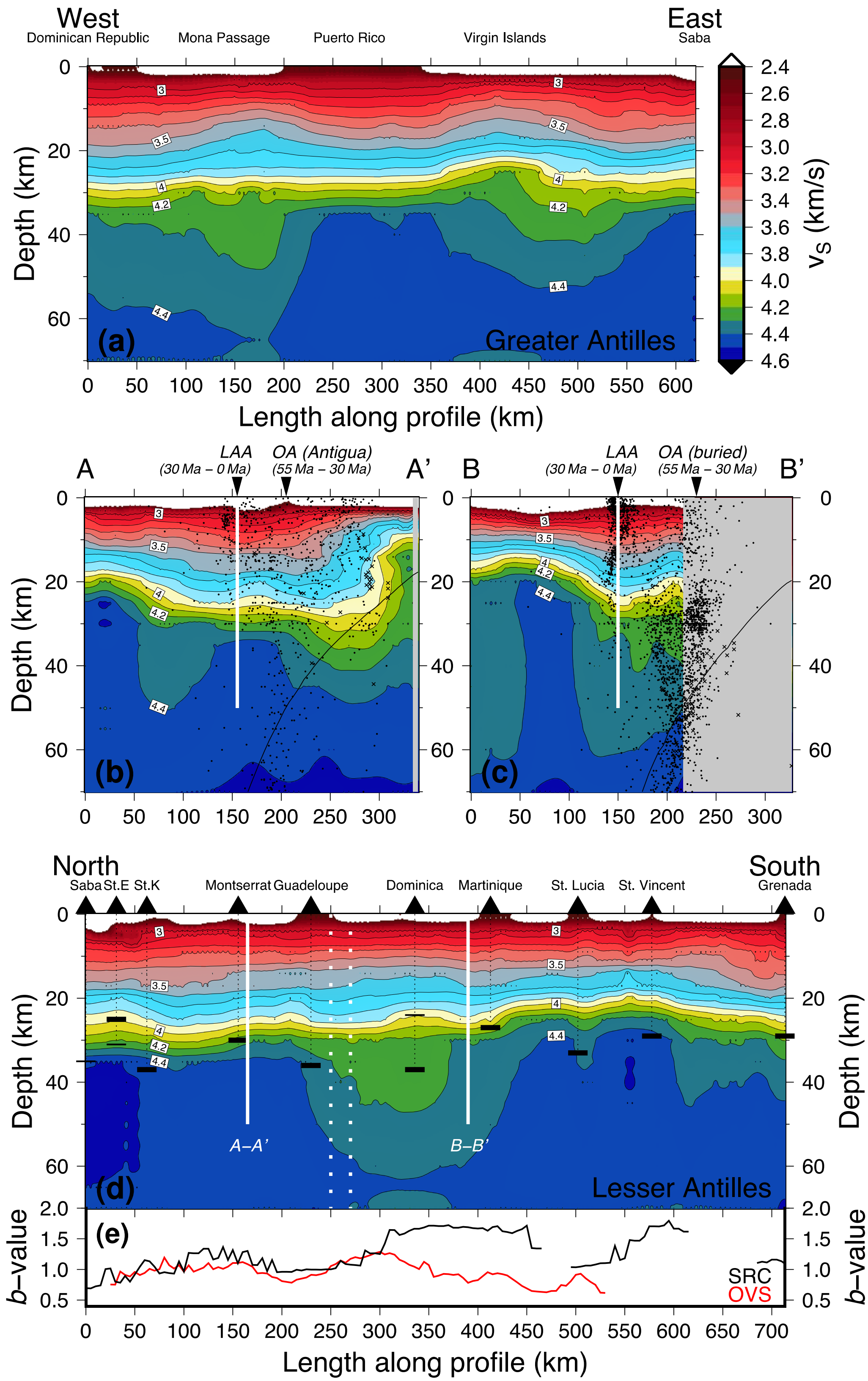

330

331 *Figure 10: see next page for caption.*

Figure 10: Velocity–depth transects along the GA (a), across the LAA (b,c), and along the LAA (d), including b*-values along the arc (e). The transect crossing positions are marked by white vertical bars. See Figure 1 for line locations. The black dots and crosses in (b,c) show all seismicity in a 30 km distance to the transect, based on the catalogue of the Institut de Physique du Globe de Paris (IPGP) from the years 1996 to 2012 and events located with the VoiLA OBS network (Bie et al., 2020), respectively. The black curved line show the location of the subducting slab based on slab2 (Hayes et al., 2018). The black inverted triangles show the positions of the LAA and the OA as the Limestone Caribbees in the north (b) and the buried OA in the south (c). The black vertical dotted lines with black horizontal bars indicate the Moho depth estimates based on Melekhova et al. (2019, thick bars), and Schlaphorst et al. (2018, thin bars) at stations where the former study did not provide results (Saba) or where the difference between both studies is greater than 1 km (St. Eustatius, Dominica). The approximate location of two major subducted fracture zones (see Figs. 1, 9) is bounded by vertical white dotted lines; uncertainties arise due to the oblique subduction angle. Lack of data results in the grey-shaded black under the western part of the crosscutting transects. The two along-arc* b*-value profiles show two different seismic catalogues (OVS – Observatoires Volcanologiques et Sismologiques of the Institut de Physique du Globe de Paris; SRC – Seismic Research Centre of The University of the West Indies) and are taken from Schlaphorst et al. (2016), see that study for further calculation details.*

Individual dispersion curves and shear velocity depth-velocity profiles (Fig. 8a,b) are highly variable depending on location. Below the arc, the shear-wave velocity generally increases from 2.5 km/s at depths shallower than 5 km to values around 4.5 km/s at depth of 25 – 35 km. In contrast, below the fore- and back-arc the velocities are slower velocities down to a depth of around 15 km. Below this depth however, velocities in the back-arc exceed the arc values, already reaching 4.5 km/s, the average value at the bottom of the model (150 km), at this depth in the southern back-arc. The pattern changes in the Mona Passage, where the shape of the velocity increase is more gradual throughout. However, the fact that the corresponding dispersion curve does not match the phase velocities within error, likely disturbed at the short-period end (14 s), points to greater and perhaps unresolved complexity in the region (Fig. 8A). Low velocity zones (LVZ) appear in many locations below 70km; they are sustained from the input model around the depth of the mantle wedge, thus increasing in thickness to the west in the LAA.

Shear velocity depth slices (Fig. 9), and along- and across-arc transects (Fig. 10) show significant changes in the crust and upper mantle. The scale used (red – light blue and afterwards yellow – green – dark blue) indicates the values typically associated with crustal (up to 3.9 km/s) and mantle (greater than 4.0 km/s) shear-wave velocity values with a light yellow layer in between to make the separation visible.

The crust is thicker beneath the GA and the LAA and thinner in the fore- and back-arc regions (Fig. 9b). Furthermore, low velocity anomalies at 20 km can also be found beneath the Aves Ridge, the remnant volcanic arc to the west of the back-arc region behind the Grenada Basin (see Fig. 1). In the southern basin, values are among the lowest of the entire study area (down to 2.58 ± 0.07 km/s) at 10 km depth but increase rapidly with depth to values among the highest at 20 km depth (up to 4.85 ± 0.04 km/s), also observable in the individual profiles (Fig. 8b). Around 30 km depth, the GA and the northern LAA show significantly lower velocity values compared to the southern LAA (4.0 – 4.2 km/s against 4.1 – 4.5 km/s; Fig. 9c). At greater depths, the area around the central LAA (roughly Guadeloupe to Martinique) shows decreased velocities to the surrounding LAA (Fig. 9d–f).

This north-south division of the LAA is also apparent in the along-arc transect, with the island of Dominica roughly marking the change (Fig. 10d). The arc crust is on average 5 km thinner in the south (20 – 25 km vs 25 – 30 km). At around 10 km depth, slightly lower velocities can be found beneath the islands in the north (Saba, St. Eustatius, St. Kitts) and the south (Grenada). In contrast, the lowest velocities at around 30 to 40 km depth can be found beneath the islands towards the centre of the arc (especially Dominica, but also Guadeloupe; Fig. 10d).

Transects crosscutting the LAA (Fig. 10b,c) generally show thicker crust beneath the arc. In the north around Montserrat the thickened crust persists many tens of kilometres into the fore- and back-arc (Fig. 10b), whereas in the central arc around Martinique the thinning occurs more abruptly (Fig. 10c). There, a low velocity region (v_S < 4.3 km/s) is apparent below 70 km creating the mantle wedge. In the cross sections the majority of crustal seismicity above the slab matches the crustal thickness derived from the tomography values (Fig. 10b,c). Furthermore, towards the forearc seismic velocities at depths between 30 km and 55 km are lower in the central arc (4.2 – 4.4 km/s) than in the northern part (4.3 – 4.5 km/s).

In the eastern part of the GA (Fig. 10a) the depth-velocity profile resembles that in the northern LAA. Mantle values around 40 km depth are higher beneath Puerto Rico, comparable to the northern and southern LAA, whereas to the west (Mona Passage, Hispaniola) and the east (Virgin Islands) the subsurface structure profile resembles more the pattern observed in the central part of the LAA.

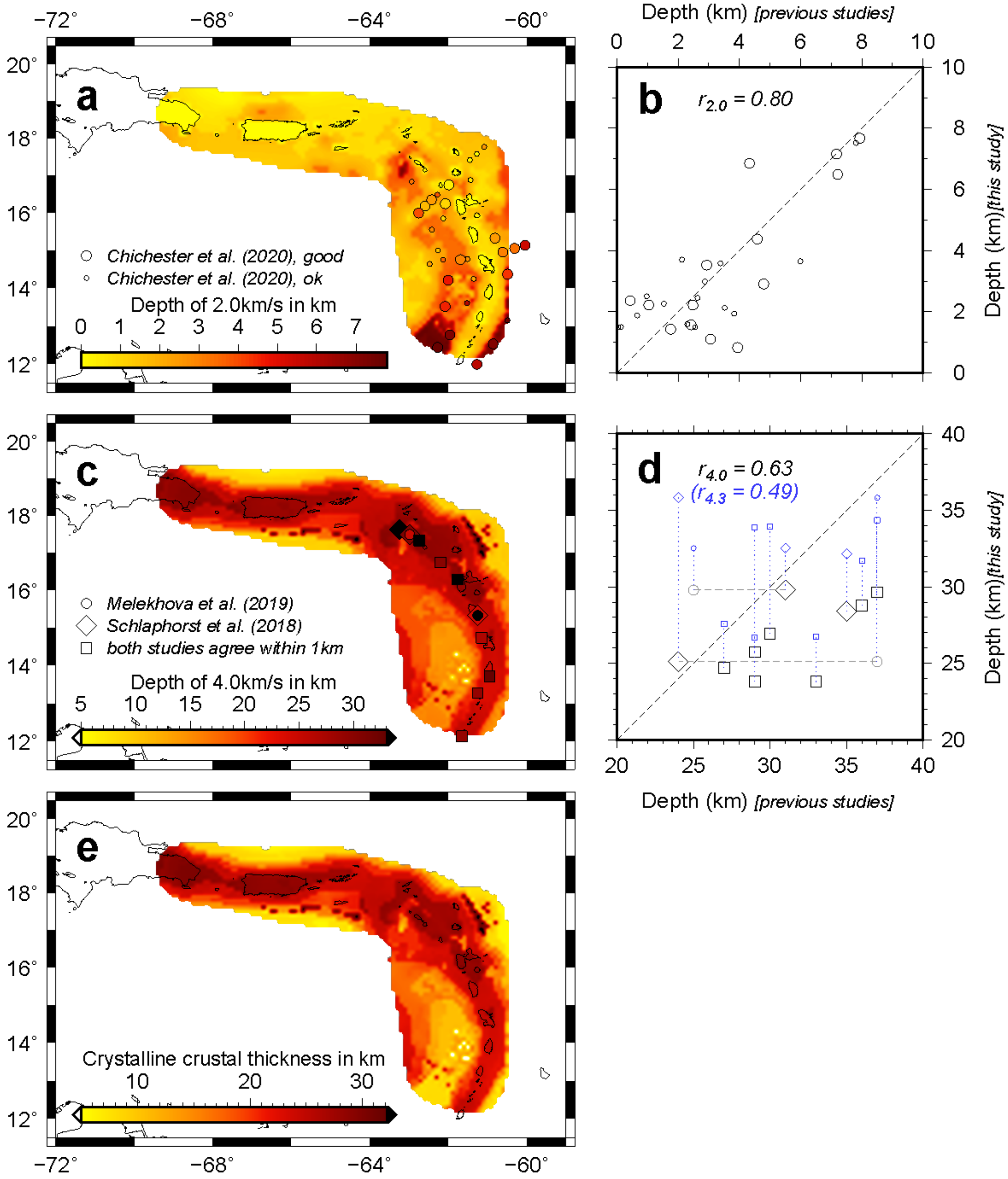

Figure 11: see next page for caption.

Figure 11: Equivelocity surfaces to map sediment layer depth and Moho depth. a) Depth of 2.0 km/s surface as an estimate of sediment limit. Circles represent depth estimates from previous study (Chichester et al., 2020), the size represent quality of the results. b) Pointwise comparison between previous and current studies, also showing the correlation coefficient ($r_{2.0}$). c) Depth of 4.0 km/s surface as an estimate of Moho depth. Diamonds, circles and squares represent depths from previous studies (Schlaphorst et al., 2018; Melekhova et al., 2019). d) Pointwise comparison between previous and current studies, also showing the correlation coefficient ($r_{4.0}$). Note that for two measurements Moho depth estimates between both previous studies differ significantly. In those cases both symbols are plotted and connected with grey hashed line. The depths of the 4.3 km/s surface at the same points are indicated by smaller blue symbols, connected by blue dotted lines and their correlation coefficient is shown in blue ($r_{4.3}$). e) Crystalline crustal thickness, calculated from difference between depths of 4.0 km/s and 2.0 km/s surfaces.

Our result may also be used to specifically map sediment and crustal thickness (Fig. 11). We choose average proxy values that are typically associated with the base of the sediment layer (2.0 km/s; Fig. 11a) and the location of the Moho (4.0km/s; Fig. 11c). We acknowledge that slightly different choices, such as gradients or other nominal velocity values are possible, but our choices compare well with estimates from previous studies of sediment thickness (Chichester et al. 2020; circles in Figs. 11a,b) and the Moho depth (Schlaphorst et al., 2018; Melekhova et al., 2019; symbols in Fig. 11c,d).

The depth to the 2.0 km/s velocity contour shows thick sedimentary loads (Fig. 11a) in the area around the southern LAA in the fore-arc (Tobago Basin) and back-arc regions (Grenada Basin) with values exceeding 7 km. In the back-arc the extent of the deepened 2.0 km/s velocity contour in the Grenada Basin can be observed as far north as the region west of Guadeloupe. There however, the sedimentary thickness decreases to values of around 4 km. The northern part of the LAA, as well as the entire GA show thinner sedimentary thicknesses, generally not exceeding 2 km. Thinner sedimentary thicknesses of less than 1 km are observed right on the Aves Ridge, the LAA and the continuation into the GA.

The depth to the 4.0km/s velocity contour shows the deepest values on the LAA and the GA (Fig. 11c) with values exceeding 25 km. The LAA shows consistently deeper values in the northern part (north of Dominica). Together with Hispaniola and the Mona Passage, the depths can be observed to reach 30 km there. In contrast, the fore- and back-arc basins show significantly shallower depths at values below 15 km, especially in the southern and central Grenada Basin.

Differencing the 4.0 km/s and the 2.0 km/s surfaces, we can calculate an estimate for the crustal thickness (Fig. 11e). The resulting map clearly shows the thicker crustal areas of the LAA, the GA and the Aves Ridge and the thinner crustal areas with minimum values reaching 10 km in the fore- and back-arc with the Grenada Basin again being the most pronounced. Maximum values reach 30 km in the northern LAA and parts of the GA and are slightly lower at around 25 km in the southern LAA and the Aves Ridge.

5 Discussion

The shear-wave velocity structures of the eastern GA and the LAA observed in this study reveal the variations in sediment and crustal thickness across the region. These results yield insights into the construction of the arc and adjacent basins, especially its tectonic history in terms of arc jumps and the influence of fracture zones and sediment subduction on the along-arc heterogeneity.

The sediment thickness we infer from the 2 km/s contour map in this study is thicker in the south in both the Grenada Basin and Tobago Basin near the South American Margin (Fig. 11a). The thickness is in general agreement with point measurements derived from scattered phases and refraction work in the region (Allen et al., 2019; Chichester et al., 2020; Padron et al., 2020), showing a correlation coefficient of $r = 0.80$, which gives confidence in the choice of this velocity as our estimated proxy (Fig. 11b). The thickening of sediment load is consistent with high sediment output from the Orinoco river and active back-arc spreading in the Paleogene (Allen et al., 2019).

In a similar way, there is general agreement between the 4.0 km/s contour depth and the crustal thickness values derived from receiver function studies and petrological constraints (Fig. 11c; Schlaphorst et al., 2018; Melekhova et al., 2019). The southern sub- arc crust is thinner than that in the north in all models (Melekhova et al. 2019; Schlaphorst et al., 2018). Our Moho depths assuming the 4.0 km/s contour are generally smaller than those from receiver functions (Fig. 11d). However, this can be explained by the difference in sensitivity between point measurements of receiver functions from phases with almost vertical incidence angles and broader lateral sensitivity of inter-station ambient noise. Still, the correlation coefficient of $r = 0.63$ hints to a positive correlation. We also compare previous results to the 4.3 km/s contour, which increases our inferred Moho depth, but also decreases the correlation coefficient (Fig. 11d). In addition, the thicker crust in the Aves Ridge and thinner crust in the Grenada and Tobago Basins (22 km vs < 10 km) agree with values found by an active source wide angle seismic profile experiment across the region (Christeson et al., 2008).

The variations in crustal thickness are likely related to the complex tectonic setting with multiple subduction fronts at the edges of the microplates in the GA, with active and relict parts of the arc in near proximity (Boschman et al, 2014). Thicker crust beneath the LAA and GA arc platforms, in comparison to areas surrounding the arc, is consistent with the notion of magmatic addition to the top and base of the Caribbean crust due to arc volcanism (Fig. 11c,e). Variation within the arc platform, e.g. the northern LAA is thicker than the Southern LAA, is likely due to the presence of the OA, which was active 55 to 30 Ma when the Grenada Basin was opening in the south (Allen et al., 2019). In other words, the arc platform in the northern LAA is thicker due to more sustained, but laterally varying arc volcanism (Wadge, 1984). The crystalline crustal thickness inferred by differencing the depth between the 2.0 km/s and 4.0 km/s contour in the southern Grenada and Tobago Basins implies southward thinning to < 8 km (Fig 11e). This is consistent with past back-arc extension until ~8 Ma (Allen et al., 2019). The northern part of the Grenada Basin appears to be made of stretched arc material with no back arc spreading, leading to the bulbous shape of the OA in the south LAA and larger distances between the LAA and the OA (Figs. 1,10B,C; Allen et al., 2019; Padron et al., 2020). This pinning of the arc position in the north was due to differential boundary forces with the American plates.

Velocity variations at 30 to 60 km depth, likely the upper mantle, are in general agreement with previous results. The pronounced section of low velocity (< 4.4 km/s) beneath Guadeloupe to Martinique is consistent with noise tomography using the permanent land stations (Arnaiz-Rodríguez et al., 2020) and also the teleseismic study using the same data set used here (Cooper et al., 2020).

Variations in upper plate mantle velocities also reveal additional insight into the dynamics of the system and in particular the relationship between the wedge and arc volcanism. Slow velocities beneath the north-central arc (Guadeloupe, Dominica and Martinique) at 30 to 60 km depth, and to a lesser extent beneath the Grenadines and Grenada at 30 to 40 km are all located in regions of thickened crust, interpreted based on the 4.0 km/s velocity contour. These anomalies could be caused by upwelling of hot mantle material and/or a small amount of partial melt and fluids, potentially caused by flux melting and/or decompression melting. The along-arc heterogeneities are observed on small length scales (tens of kilometres), which is also observed in changes of characteristics such as mantle xenolith mineral composition (Melekhova et al., 2019).

The variable seismic velocities in the upper plate are likely influenced by the release of fluids from the slab. The low velocity zone in the mantle wedge beneath Guadeloupe and Martinique is bounded by two major fracture zones to the north, which also lie near the boundary of the proto-Caribbean/equatorial Atlantic seafloor boundary (Cooper et al., 2020; Harmon et al., 2019). The *b*-values of slab earthquakes (Schlaphorst et al., 2016) are also higher in the forearc offshore of Dominica and Martinique, in close proximity to our seismic anomaly, suggesting greater fluid release in this part of the subduction zone. The higher *b*-values also coincide with a region of lower seismic velocity on the slab from local earthquake and active source tomography (Paulatto et al., 2017). The high $\delta^{11}B$ anomaly in erupted magmas from Guadeloupe and Dominica, indicative of dewatering of serpentinized oceanic crust, occurs just north of that region, closer to the fracture zones on the slab in the north that bisect Guadeloupe and Martinique (Cooper et al., 2020). In addition, pre-existing faults from the formation at the ridge can open via bending during the subduction process, thus allowing for further hydration. However, the lack of intraslab, trench-parallel normal fault focal mechanisms from earthquakes in the forearc and outer rise makes this process unlikely to have a dominant role. Therefore, an alternative explanation is that there is three dimensional flow owing to the curvature of the arc or gaps in the slab. Similarly, ponding melt could redistribute fluids and/or melt between the slab and the arc (Ha et al., 2020). Linked to that, the most productive volcanoes over the last 100 kyr can be found on Dominica (Wadge, 1984). Another possibility is that along-strike variability in the morphology of the subducted seafloor itself can have an impact on the velocity structure. For instance, oceanic core complexes, that are formed in slow- and intermediate-spreading environments, at times when magma supply is limited (Smith et al., 2008) may cause crustal alteration, based on slow seismic velocities outboard on the incoming plate of our study area (Davy et al., 2019).

Further north, the lower velocities throughout the upper mantle between Hispaniola and Puerto Rico (Fig. 10a) occur in a region with moderate interpreted crustal thickness (close to 30 km). The anomaly is interesting and potentially different to the rest of the arc where low upper mantle velocities are associated with thickened crust and an active volcanic arc. This anomaly could arise due to the ongoing opening of the Mona Passage (Jansma et al., 2005). In other words, the extensional tectonics may cause upwelling of hotter, potentially more hydrated mantle material from depth, possibly also associated with decompression melting.

6 Conclusions

In this study we used ambient noise tomography to map crustal and upper mantle shear-wave velocity of the eastern GA and the LAA using data from permanent land stations and from ocean bottom seismometers collected as part of VoiLA experiment in 2016/17. We observe significant along-arc heterogeneities on small length scales (~50 km) that agree with heterogeneities of a variety of characteristics such as mantle xenolith mineral composition and discontinuity structure (including crustal thickness) variation, changes in sediment and water subduction, as well as melt generation distribution observed by previous studies. Our estimates of sedimentary basin and crustal thickness agree with point measurements and profiles throughout the LAA from previous modelling of receiver functions, petrology, and active source studies. We observe increased sediment thickness (> 7 km) in the southern fore- (Tobago Basin) and back-arc regions (Grenada Basin). This can be explained by sediment supply from the Orinoco and active back-arc spreading in the Paleogene. The crust is thicker beneath the GA and the northern LAA islands, reaching values of around 30 km. The LAA south of Dominica shows smaller crustal thickness values of 20 to 25 km. In the fore-arc, where the older arc has been buried under the thick Barbados sediments (Allen et al., 2019), and in the back-arc regions in the Grenada Basin, crustal thickness are as low as 10 km. Along the arc, shear-wave velocities in the upper mantle are significantly lower beneath the Mona Passage, as well as beneath the central LAA from Guadeloupe to Martinique (4.2 – 4.4 km/s). This can be explained by upwelling of hot mantle material or a small amount of partial melt, or both, and is likely caused by flux or decompression melting or a combination of these. The subduction of the proto-Caribbean/equatorial Atlantic seafloor boundary at two major fracture zones are located just north of the anomaly that runs from Guadeloupe to Martinique. Therefore, three dimensional flow because of slab curvature and/or a gap in the slab, seafloor morphology such as oceanic core complexes, and/or melt ponding with potential influences from the overriding plate (or a combination of those) are likely to have a dominant impact on the location and degree of arc volcanism in the area. In general, slow spreading ridges, in our case the MAR, lead to high amount of hydration with high along-arc variability. This results in the slow subduction of highly heterogeneous slab hydration patterns that facilitate the variable crustal and upper mantle structure we observed.

Acknowledgments, Samples, and Data

This research was funded by the VoiLA NERC consortium grant (NE/K010824/1). We thank all who sailed on cruises RRS James Cook JC133 and JC149. We thank our partners at the University of West Indies Seismic Research Centre (SRC), in particular Lloyd Lynch, Kemron Alexander, Richard Robertson and Joan Latchman as well as Laura Petrescu and Ben Chichester for support with island station installation, the German Instrument Pool for Amphibian Seismology (DEPAS), hosted by the Alfred Wegener Institute Bremerhaven for providing the ocean-bottom and temporary island seismometers, and UCSD (Scripps) for providing additional ocean-bottom seismometers. DS would like to acknowledge the financial support FCT through project UIDB/50019/2020 – IDL. Data used in this project is available from the IRIS DMC (www.iris.edu/dmc) and we used of data from the following Networks: CU (https://doi.org/10.7914/SN/CU), G (https://doi.org/10.18715/GEOSCOPE.G), IU (https://doi.org/10.7914/SN/IU), NA (https://doi.org/10.21944/dffa7a3f-7e3a-3b33-a436-516a01b6af3f), PR (https://doi.org/10.7914/SN/PR), TR (No Doi), WI (https://doi.org/10.18715/antilles.WI), and XZ (https://doi.org/10.7914/SN/XZ_2016).

References

Allen, R. W., Collier, J. S., Stewart, A. G., Henstock, T., Goes, S., Rietbrock, A., & VoiLA Team. (2019), The role of arc migration in the development of the Lesser Antilles: A new tectonic model for the Cenozoic evolution of the eastern Caribbean. *Geology*, 47(9), 891–895. doi: 10.1130/G46708.1

Arnaiz-Rodríguez, M. S., Schmitz, M., & Audemard, F. (2016), La estructura cortical del arco de las Antillas Menores estimada a partir de la técnica de funciones receptoras. *Revista mexicana de ciencias geológicas*, 33(3), pp.286–296.

Arnaiz-Rodríguez, M. S., Zhao, Y., Sánchez-Gamboa, A.K., & Audemard, F. (2020), Crustal and upper-mantle structure of the Eastern Caribbean and Northern Venezuela from passive Rayleigh wave tomography. *Tectonophysics*, p.228711. doi: 10.1016/j.tecto.2020.228711

Becker, J. J., Sandwell, D. T. , Smith, W. H. F., Braud, J., Binder, B., Depner, J., et al. (200), Global Bathymetry and Elevation Data at 30 Arc Seconds Resolution: SRTM30_PLUS, *Marine Geodesy*, 32:4, 355–371, doi: 10.1080/01490410903297766

Bensen, G.D., Ritzwoller, M. H., Barmin, M. P., Levshin, A. L., Lin, F., Moschetti, M.P., Shapiro, N.M., & Yang, Y. (2007). Processing seismic ambient noise data to obtain reliable broad-band surface wave dispersion measurements. *Geophysical Journal International*, 169(3), pp.1239–1260. doi: 10.1111/j.1365-246X.2007.03374.x

Bie, L., Rietbrock, A., Hicks, S., Allen, R., Blundy, J., Clouard, V., et al. (2020), Along-Arc Heterogeneity in Local Seismicity across the Lesser Antilles Subduction Zone from a Dense Ocean-Bottom Seismometer Network. *Seismological Research Letters*, 91(1), pp.237–247. doi: 10.1785/0220190147

Boschman, L. M., van Hinsbergen, D. J., Torsvik, T. H., Spakman, W., & Pindell, J. L. (2014), Kinematic reconstruction of the Caribbean region since the Early Jurassic. *Earth-Science Reviews*, 138, pp.102–136. doi: 10.1016/j.earscirev.2014.08.007

Bouysse, P., Westercamp, D. and Andreieff, P. (1986), 4. The Lesser Antilles Island Arc. In *Proceedings of the Ocean Drilling Program: Scientific results* (Vol. 110, p. 29). The Program.

Boynton, C. H., Westbrook, G. K., Bott, M. H. P. & Long, R. E. (1979), A seismic refraction investigation of crustal structure beneath the Lesser Antilles island arc. *Geophysical Journal International*, 58(2), pp.371–393. doi: j.1365-246X.1979.tb01031.x

Cai, C., Wiens, D.A., Shen, W. & Eimer, M., 2018. Water input into the Mariana subduction zone estimated from ocean-bottom seismic data. *Nature*, 563(7731), pp.389–392. doi: 10.1038/s41586-018-0655-4

Campillo, M., Roux, P. & Shapiro, N. M. 2011. Using seismic noise to image and to monitor the Solid Earth. *Encyclopedia of Solid Earth Geophysics*, pp.1230–1235.

Chichester, B., Rychert, C., Harmon, N., Collier, J., Henstock, T., Goes, S.D., et al. (2019), Seismic imaging of the Lesser Antilles subduction zone using S-to-P receiver functions. In *AGU Fall Meeting Abstracts* (Vol. 2019, pp. S53C-0521).

Chichester, B., Rychert, C., Harmon, N., Allen, R., Collier, J., Henstock, T., & Rietbrock, A. (2020). Seafloor sediment thickness beneath the VoiLA broadband ocean-bottom seismometer deployment in the Lesser Antilles from P-to-S delay times. *Geophysical Journal International*. doi: 10.1093/gji/ggaa360

Christeson, G.L., Mann, P., Escalona, A., & Aitken, T. J. (2008). Crustal structure of the Caribbean–northeastern South America arc-continent collision zone. *Journal of Geophysical Research: Solid Earth*, 113(B8). doi: 10.1029/2007JB005373

Collier, J.S. (2017), VoiLA—Volatile recycling in the Lesser Antilles arc: RRS James Cook cruise report JC149. Imperial College London, https://www. bodc. ac. uk/resources/inventories/cruise_inventory/reports/jc149. pdf, pp.1–161.

Cooper, G. F., Macpherson, C. G., Blundy, J. D., Maunder, B., Allen, R. W., Goes, S., et al. (2020), Variable water input controls evolution of the Lesser Antilles volcanic arc. *Nature*, 582(7813), 525–529. doi: 10.1038/s41586-020-2407-5

Davy, R. G., Collier, J. S., Henstock, T. J., & VoiLA Consortium. (2020), Wide-angle seismic imaging of two modes of crustal accretion in mature Atlantic Ocean crust. *Journal of Geophysical Research: Solid Earth*, 125(6), p.e2019JB019100. doi: 10.1029/2019JB019100

DeMets, C., Jansma, P. E., Mattioli, G. S., Dixon, T. H., Farina, F., Bilham, R., et al. (2000), GPS geodetic constraints on Caribbean-North America plate motion. *Geophysical Research Letters*, 27(3), pp.437–440. doi: 10.1029/1999GL005436

Dolan, J. F., Mullins, H. T., Wald, D. J., & Mann, P. (1998), Active tectonics of the north-central Caribbean: Oblique collision, strain partitioning, and opposing subducted slabs. *Special Papers-Geological Society of America*, pp.1–62.

Faugères, J. C., Gonthier, E., Griboulard, R., & Masse, L. (1993), Quaternary sandy deposits and canyons on the Venezuelan margin and south Barbados accretionary prism. *Marine Geology*, 110(1-2), pp.115–142. doi: 10.1016/0025-3227(93)90109-9

Goes S., Collier J., Blundy J., Davidson J., Harmon N., Henstock T., et al. (2019), Project VoiLA: Volatile Recycling in the Lesser Antilles, *Eo*s, 100, ISSN:2324–9250

Ha, G., Montési, L.G., & Zhu, W. (2020), Melt Focusing Along Permeability Barriers at Subduction Zones and the Location of Volcanic Arcs. *Geochemistry, Geophysics, Geosystems*, 21(12), p.e2020GC009253. doi: 10.1029/2020GC009253

Harmon, N., Gerstoft, P., Rychert, C. A., Abers, G. A., Salas de La Cruz, M., & Fischer, K. M. (2008), Phase velocities from seismic noise using beamforming and cross correlation in Costa Rica and Nicaragua. *Geophysical Research Letters*, 35(19). doi: 10.1029/2008GL035387

Harmon, N., Rychert, C. A., & Gerstoft, P. (2010), Distribution of noise sources for seismic interferometry. *Geophysical Journal International*, 183(3), pp.1470–1484. doi: 10.1111/j.1365-246X.2010.04802.x

Harmon, N., & Rychert, C. A. (2016), Joint inversion of teleseismic and ambient noise Rayleigh waves for phase velocity maps, an application to Iceland. *Journal of Geophysical Research: Solid Earth*, 121(8), pp.5966–5987. doi: 10.1002/2016JB012934

Harmon, N., Rychert, C. A., Collier, J., Henstock, T., van Hunen, J., & Wilkinson, J.J. (2019), Mapping geologic features onto subducted slabs. *Geophysical Journal International*, 219(2), pp.725–733. doi: 10.1093/gji/ggz290

Hayes, G.P., Moore, G.L., Portner, D.E., Hearne, M., Flamme, H., Furtney, M., & Smoczyk, G.M. (2018), Slab2, a comprehensive subduction zone geometry model. *Science*, 362(6410), pp.58–61. doi: 10.1126/science.aat4723

Kopp, H., Weinzierl, W., Becel, A., Charvis, P., Evain, M., Flueh, E. R., et al. (2011), Deep structure of the central Lesser Antilles Island Arc: relevance for the formation of continental crust. *Earth and Planetary Science Letters*, 304(1-2), pp.121–134. doi: 10.1016/j.epsl.2011.01.024

Jansma, P. E., Mattioli, G. S., & Mann, P. (2005), GPS results from Puerto Rico and the Virgin Islands: Constraints on tectonic setting and rates of active faulting. *Active Tectonics and Seismic Hazards of Puerto Rico, the Virgin Islands, and Offshore Areas* 385, pp. 13–30

Lin, F. C., Ritzwoller, M. H., & Shapiro, N. M. (2006), Is ambient noise tomography across ocean basins possible?. *Geophysical Research Letters*, 33(14). doi: 10.1029/2006GL026610

Lin, F. C., Ritzwoller, M. H., Townend, J., Bannister, S., & Savage, M. K. (2007), Ambient noise Rayleigh wave tomography of New Zealand. *Geophysical Journal International*, 170(2), pp.649–666. doi: 10.1111/j.1365-246X.2007.03414.x

Lin, F. C., Ritzwoller, M. H., & Snieder, R. (2009), Eikonal tomography: surface wave tomography by phase front tracking across a regional broad-band seismic array. *Geophysical Journal International*, 177(3), pp.1091–1110. doi: 10.1111/j.1365-246X.2009.04105.x

Masson, D. G., & Scanlon, K. M. (1991), The neotectonic setting of Puerto Rico. *Geological Society of America Bulletin*, 103(1), pp.144–154. doi: 10.1130/0016-7606(1991)103<0144:TNSOPR>2.3.CO;2

Meighan, H. E., & Pulliam, J. (2013), Seismic anisotropy beneath the northeastern Caribbean: Implications for the subducting North American lithosphere. *Bulletin de la Société Géologique de France*, 184(1-2), pp.67–76. doi: 10.2113/gssgfbull.184.1-2.67

Melekhova, E., Schlaphorst, D., Blundy, J., Kendall, J. M., Connolly, C., McCarthy, A., & Arculus, R. (2019), Lateral variation in crustal structure along the Lesser Antilles arc from petrology of crustal xenoliths and seismic receiver functions. *Earth and Planetary Science Letters*, 516, pp.12–24. doi: 10.1016/j.epsl.2019.03.030

Mordret, A., Shapiro, N. M., Singh, S. S., Roux, P., & Barkved, O.I. (2013a), Helmholtz tomography of ambient noise surface wave data to estimate Scholte wave phase velocity at Valhall Life of the FieldNoise tomography at Valhall. *Geophysics*, 78(2), pp.WA99–WA109. doi: 10.1190/geo2012-0303.1

Mordret, A., Landès, M., Shapiro, N.M., Singh, S. C., Roux, P., & Barkved, O.I., (2013b), Near-surface study at the Valhall oil field from ambient noise surface wave tomography. *Geophysical Journal International*, 193(3), pp.1627–1643. doi: 10.1093/gji/ggt061

Mordret, A., Landès, M., Shapiro, N. M., Singh, S. C., & Roux, P. (2014), Ambient noise surface wave tomography to determine the shallow shear velocity structure at Valhall: depth inversion with a Neighbourhood Algorithm. *Geophysical Journal International*, 198(3), pp.1514–1525. doi: 10.1093/gji/ggu217

Padron, C., Klingelhoefer, F., Marcaillou, B., Lebrun, J. F., Lallemand, S., Garrocq, C., et al. (2018), Deep structure of the Grenada Basin from wide-angle seismic, bathymetric and gravity data. *Journal of Geophysical Research: Solid Earth*, p.e2020JB020472. doi: 10.1029/2020JB020472

Ritzwoller, M. H., Lin, F. C., & Shen, W. (2011), Ambient noise tomography with a large seismic array. *Comptes Rendus Geoscience*, 343(8-9), pp.558–570. doi: 10.1016/j.crte.2011.03.007

Sabra, K. G., Gerstoft, P., Roux, P., Kuperman, W. A., & Fehler, M. C. (2005), Extracting time-domain Green's function estimates from ambient seismic noise. *Geophysical Research Letters*, 32(3). doi: 10.1029/2004GL021862

Schlaphorst, D., Kendall, J. M., Collier, J. S., Verdon, J. P., Blundy, J., Baptie, B., et al. (2016), Water, oceanic fracture zones and the lubrication of subducting plate boundaries—insights from seismicity. *Geophysical Journal International*, 204(3), pp.1405–1420. doi: 10.1093/gji/ggv509

Schlaphorst, D., Kendall, J. M., Baptie, B., Latchman, J. L., & Tait, S. (2017), Gaps, tears and seismic anisotropy around the subducting slabs of the Antilles. *Tectonophysics*, 698, pp.65–78. doi: 10.1016/j.tecto.2017.01.002

Schlaphorst, D., Melekhova, E., Kendall, J. M., Blundy, J., & Latchman, J. L. (2018), Probing layered arc crust in the Lesser Antilles using receiver functions. *Royal Society Open Science*, 5(11), p.180764. doi: 10.1098/rsos.180764

Shapiro, N. M., & Campillo, M. (2004), Emergence of broadband Rayleigh waves from correlations of the ambient seismic noise. *Geophysical Research Letters*, 31(7). doi: 10.1029/2004GL019491

Shapiro, N. M., Campillo, M., Stehly, L., & Ritzwoller, M. H. (2005), High-resolution surface-wave tomography from ambient seismic noise. *Science*, 307(5715), pp.1615–1618. doi: 10.1126/science.1108339

Smith, D. K., Escartín, J., Schouten, H., & Cann, J. R. (2008), Fault rotation and core complex formation: Significant processes in seafloor formation at slow-spreading mid-ocean ridges (Mid-Atlantic Ridge, 13–15 N). *Geochemistry, Geophysics, Geosystems*, 9(3). doi: 10.1029/2007GC001699

Stern, R. J. (2002), Subduction zones. *Reviews of Geophysics*, 40(4), pp.3-1. doi: 10.1029/2001RG000108

Stewart, P. (2006), Interferometric imaging of ocean bottom noise. In SEG Technical Program Expanded Abstracts 2006(pp. 1555–1559). *Society of Exploration Geophysicists*. doi: 10.1190/1.2369817

Ten Brink, U. (2005), Vertical motions of the Puerto Rico Trench and Puerto Rico and their cause. *Journal of Geophysical Research: Solid Earth*, 110(B6). doi: 10.1029/2004JB003459

Wadge, G. (1984), Comparison of volcanic production rates and subduction rates in the Lesser Antilles and Central America. *Geology*, 12(9), pp.555–558. doi: 10.1130/0091-7613(1984)12<555:COVPRA>2.0.CO;2

Wadge, G., & Shepherd, J. B. (1984), Segmentation of the Lesser Antilles subduction zone. *Earth and Planetary Science Letters*, 71(2), pp.297–304. doi: 10.1016/0012-821X(84)90094-3

Yang, Y., Ritzwoller, M. H., Levshin, A. L., & Shapiro, N. M. (2007), Ambient noise Rayleigh wave tomography across Europe. *Geophysical Journal International*, 168(1), pp.259–274. doi: 10.1111/j.1365-246X.2006.03203.x

Yang, Y., & Ritzwoller, M. H. (2008), Characteristics of ambient seismic noise as a source for surface wave tomography. *Geochemistry, Geophysics, Geosystems*, 9(2). doi: 10.1029/2007GC001814